

FULL ARTICLE

Well-dispersed Au nanoparticles prepared via magnetron sputtering on TiO₂ nanotubes with unprecedentedly high activity for water splitting

Nada Atef | Salma S. Emara | Dina S. Eissa | Ahmed El-Sayed |
Omar A. M. Abdelraouf | Nageh K. Allam 

Energy Materials Laboratory, School of Sciences and Engineering, The American University in Cairo, New Cairo, Egypt

Correspondence

Nageh K. Allam, Energy Materials Laboratory, School of Sciences and Engineering, The American University in Cairo, New Cairo 11835, Egypt.

Email: nageh.allam@aucegypt.edu

Abstract

We report on the fine tuning of sputtered gold nanoparticles (Au NPs) with optimized diameters (7–25 nm) and distribution on the high surface area titania nanotube arrays (TNTs). The uniform coverage of Au NPs both outside and inside the nanotube arrays was possible by adjusting the sputtering current, as confirmed via scanning electron microscopy imaging and X-ray diffraction analysis. Decorating the TNTs with Au NPs extended their optical activity to the visible region of the light spectrum. This red shift was attributed to the localized surface plasmon resonance (LSPR) of Au NPs as verified computationally and experimentally. The Au–TiO₂ composites demonstrated 86% increase in the photocurrent compared to the bare TNTs upon their use as photoanodes for water splitting. The photoactivity was found to depend on the size of the sputtered Au NPs. The photocurrent transient measurements under light on/off conditions revealed the photostability of the Au–TiO₂ nanocomposites. The Mott–Schottky analysis showed a negative shift in the flat band position of the Au–TiO₂ electrodes with increased donor density compared to the bare TNTs. Moreover, the Au–TiO₂ showed lower space charge capacitance and longer life time of charge carriers.

KEYWORDS

anodization, LSPR, Mott–Schottky, nanotubes, photocurrent transients, water splitting

1 | INTRODUCTION

Climate change makes it essential to discover alternatives to fossil resources for energy needs. In this regard, the alternative technologies should align with the sustainable development goals put forward by the United Nations,

which include the importance to provide clean and affordable energy to everyone.^[1] Consequently, the production of fuels from renewable sources has the potential not only to reduce CO₂ emissions but also to do so sustainably and equitably.^[1] In this regard, the use of semiconductors and sunlight to split water to generate hydrogen is a viable way

This is an open access article under the terms of the [Creative Commons Attribution](https://creativecommons.org/licenses/by/4.0/) License, which permits use, distribution and reproduction in any medium, provided the original work is properly cited.

© 2020 The Authors. *Electrochemical Science Advances* published by Wiley-VCH GmbH

for producing synthetic fuels and chemicals. However, the core scientific challenges associated with the realization of the production of such promising source of energy lie in the identification of photocatalytically active electrode materials with optimum structure and morphology. Thus, recent advances in nanotechnology have contributed largely in developing efficient and innovative approaches for the synthesis of well-organized nanostructured materials that can be readily available for various applications. That includes the synthesis of nanotubes,^[2–4] nanowires,^[5,6] nanoparticles (NPs),^[7,8] and other nanocomposites,^[5,9,10] which have been fabricated on large scale to address the current needs of the industrial applications. Among those materials, metal oxides have been intensively investigated as photoelectrodes to split water due to their abundance, low cost, ease of fabrication, tunable bandgaps with appropriate band-edge positions, and exceptional chemical stability.^[4,11–15] However, their wide bandgap energy limits their optical activity to the ultraviolet spectrum, which represents only a small fraction (3–5%) of the overall available solar energy radiation.^[4,16]

Consequently, various approaches have been investigated to extend the photo response of metal oxides to the visible region of the light spectrum, such as doping with metals or nonmetals, sensitization with quantum dots or organic dyes, or coupling with other semiconductors.^[17–20] However, most of these attempts showed limited success to extend the absorption to the visible region, resulting in an insignificant improvement in their photoactivity. Moreover, the relatively fast recombination of charge carriers and low charge separation efficiency occurring in pristine metal oxides would further weaken their photocatalytic performance. Therefore, it is highly desirable to find a facile and efficient approach to simultaneously resolve these two crucial challenges.

For a long time, Au was assumed to be a noble element with poor catalytic activity until it was first demonstrated that Au nanoclusters supported on anatase titania have excellent catalytic activity for CO oxidation at only 200 K.^[21] Consequently, a plethora of methods have been used for the assembly of Au NPs on TiO₂ thin films with exceptional catalytic properties reported for CO to CO₂ oxidation.^[22] The maximum oxidation rate was reported for Au NPs with diameters of ca. 3.5 nm, which was ascribed to the localized surface plasmon resonance (LSPR) effect of Au NPs.^[23] Consequently, the Au NPs/TiO₂ hybrid has been investigated for many applications in photonics and sensing. The use of Au NPs was found to decrease the recombination of charge carriers in TiO₂ and increase the optical path length of incident light.^[23] Moreover, attaching Au NPs to nanostructured TiO₂ was shown to enhance TiO₂ photoactivity

by extending its absorption to the visible region and facilitating the separation of e⁻/h⁺ pairs created at the metal–semiconductor interface.^[24] The prepared Au–TiO₂ nanocomposites, by electrophoretic deposition of Au NPs on TiO₂ nanoporous films, showed a large increase in photocurrent from 0.01 mA/cm² for the unmodified TiO₂ films to 0.20 mA/cm² for Au–TiO₂ films, which was attributed to the harvesting of hot electrons from Au NPs to TiO₂.^[24] A slightly higher photocurrent density of 0.22 mA/cm² was reported for 3 μm thick Au–TiO₂ films^[25] and 0.153 mA/cm² photocurrent density after sputtering Au particles on TiO₂.^[26] Also, Au NPs supported on TiO₂ was used for the reduction of *p*-nitrophenol, which showed an increase in the dye degradation rate with decreasing the Au NP size.^[27] Moreover, the plasmonic effect of Au NPs on the photocatalytic performance of carbon shell-coated TiO₂ was investigated, which showed enhanced visible light absorption, charge separation efficiency, and transfer of photogenerated electrons and holes, making the material a promising candidate for degradation of organic pollutants.^[28]

As the active surface area of the support material directly impacts the performance of the catalytic pathways, it is expected that high available surface area will result in enhanced catalytic performance. Herein, we demonstrate a facile and simple method for decorating the high surface area TiO₂ nanotube arrays (TNTs) with Au NPs using magnetron sputtering at different deposition currents. The sputtering process was tuned to optimize the Au particle distribution and size to achieve the maximum photocurrent density upon their use for water splitting. Uniform coverage has been achieved inside, outside, and around tubes mouth with excellent control over the diameter ranging from 7 to 25 nm. For practical applications, two specific criteria are very promising: (a) assembly of Au NPs with small diameters (~10 nm) is optimum for photocatalytic applications; (b) the assembly of coherent Au NPs metallic thin layer to almost cover the entire nanotubes surfaces upon increasing the deposition current demonstrates the ability to construct localized Schottky barriers for current control. The LSPR effect of Au NPs was also studied using finite difference time domain (FDTD) modeling.

2 | MATERIALS AND METHODS

2.1 | Materials and chemicals

Ammonium fluoride (NH₄F) (Sigma Aldrich), ethylene glycol purity 99% purchased from Sigma Aldrich, acetone and ethanol purchased from ElGomhorya, Cairo, Egypt, potassium hydroxide (KOH) purchased from Sigma Aldrich, and titanium foil of thickness 0.25 mm (Sigma

Aldrich) were the raw materials for our study. All chemicals were used as received without further purification. All experiments were performed at room temperature ($22 \pm 2^\circ\text{C}$) using distilled water.

2.2 | Materials fabrication

Prior to anodization, Ti foil specimens ($2\text{ cm} \times 1\text{ cm}$) were mechanically polished, followed by ultrasonic cleaning with acetone, distilled water, and ethanol each for 5 min, respectively. Then, the foil was rinsed with distilled water and dried in atmospheric air. A direct current power supply was used as the voltage source to drive the anodization process. Anodization was performed in a two-electrode configuration with titanium foil as the anodic electrode and platinum foil as the cathodic electrode under constant potential of 40 V for 2 h. The used electrolyte was ethylene glycol-based electrolyte containing 0.3 M NH_4F and 2 vol.% H_2O . After anodization, the samples were rinsed thoroughly with distilled water. The as-anodized samples were annealed in air for 1 h at 450°C with a heating and cooling rate of $1^\circ\text{C}/\text{min}$. After annealing, different samples were sputtered using Magnetron sputtering coating unit E5000 under vacuum with Au at different deposition currents of 10, 20, and 30 mA to vary the Au NPs density, distribution, and size, while keeping the deposition time constant for 2 min.

2.3 | Characterization and measurements

The morphology of the fabricated materials was examined using a Zeiss SEM Ultra 60 field emission scanning electron microscope (FESEM). The crystal structure was investigated by recording the X-ray diffraction (XRD) spectra using a PANalytical X'Pert PRO XRD diffractometer. The optical profiles of the samples were investigated using a Shimadzu UV-Vis-NIR spectrophotometer equipped with a solid-sample holder and an integrating sphere for reflectance measurements. The photoelectrochemical measurements were performed in a three-electrode cell configuration in 1.0 M KOH aqueous solution using Ag/AgCl reference electrode, a platinum counter electrode, and the active material as the working electrode using a Bio-Logic SP 200 workstation, and sunlight was simulated using 300 W Xenon lamp (Ozone-free) under $100\text{ mW}/\text{cm}^2$ illumination equipped with AM 1.5G filter. Optical model for bare titanium (Ti) film, titanium dioxide (TiO_2) nanotubes, and TiO_2 nanotubes decorated with gold (Au) layer was constructed to calculate the total light absorption enhancement and electric field profile using

COMSOL Multiphysics. The optical refractive index of Ti, TiO_2 , and Au was taken from experimental measurements. The used mesh size was lower than the lowest simulated wavelength by $10\times$ times, incident light power coming from AM 1.5G data.

3 | RESULTS AND DISCUSSION

Figure 1a shows a typical FESEM image of the annealed TiO_2 TNTs, revealing an average tube length of $2.5\ \mu\text{m}$, wall thickness ranging from 5 to 9 nm, and pore diameter ranging from 80 to 120 nm. The morphologies of TNTs sputtered with Au NPs at deposition currents of 10, 20, and 30 mA are illustrated in Figure 1b–d, respectively. While the Au NPs sputtered at 10 mA have diameters ranging from 7 to 10 nm, those sputtered at 20 and 30 mA have diameters ranging from 14 to 25 nm. The images show that Au deposition did not damage the structure of the TNTs. Moreover, it is observable that the density of gold layer deposited increases with increasing the sputtering deposition current. Note that the Au NPs were homogeneously deposited inside, outside, and on top of the TNTs without any coalescence or clustering.

The XRD analysis was recorded to elucidate the structure of the fabricated samples. Figure 2 revealed diffraction peaks at $2\theta = 25.3^\circ$, 38.3° , 48.0° , and 53.0° , corresponding to the (101), (004), (200), and (105) facets of TiO_2 , respectively.^[2–4] The XRD pattern showed that the (004) is the most intense peak, indicating a preferential growth along the {001} direction.^[6] The obtained diffraction pattern verifies the formation of pure anatase phase.^[3] Note that the sharp peaks observed at $2\theta = 40^\circ$, 44.7° , and 70.6° are characteristic of the (111), (200), and (311) plans, respectively, of the face-centered cubic crystal structure of Au metal.^[23] Therefore, the XRD pattern confirms the synthesis of Au/ TiO_2 composite (JCPDS card no. 01-1164).

To elucidate the optical properties of the fabricated materials, the room temperature UV-Vis diffuse reflectance spectra were recorded and analyzed as depicted in Figure 3. Note that each material exhibits a sharp absorption edge at ca. 350 nm, which is the characteristic absorption signature of pure titania.^[29] However, the TNTs decorated with Au NPs show extended absorption from 400 to 800 nm, with absorption maxima within the visible region ranging from 500 to 600 nm. These absorption maxima can be ascribed to the LSPR of Au NPs. However, this plasmon absorption is red-shifted compared to colloidal Au NPs, which can be ascribed to the surrounding TiO_2 medium, indicating the high sensitivity of the surface plasmon band to the cluster-matrix interface properties. Interfacial and interparticle interactions cause the broadening and shift of the plasmon

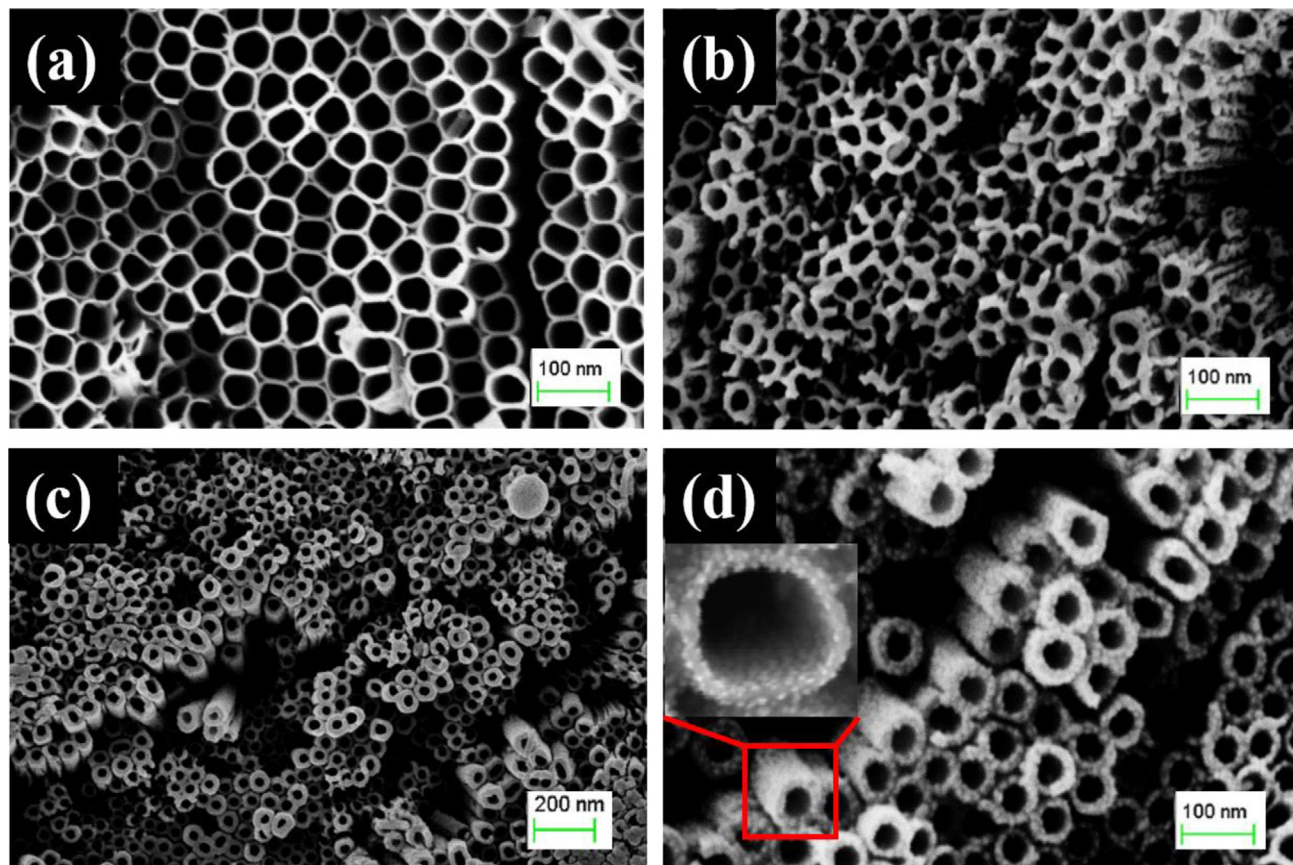


FIGURE 1 FESEM images for bare and Au-sputtered TNTs. (a) Bare TiO_2 nanotubes after Au sputtering at (b) 10, (c) 20, and (d) 30 mA. The inset is a magnified image showing the homogeneous distribution of Au NPs

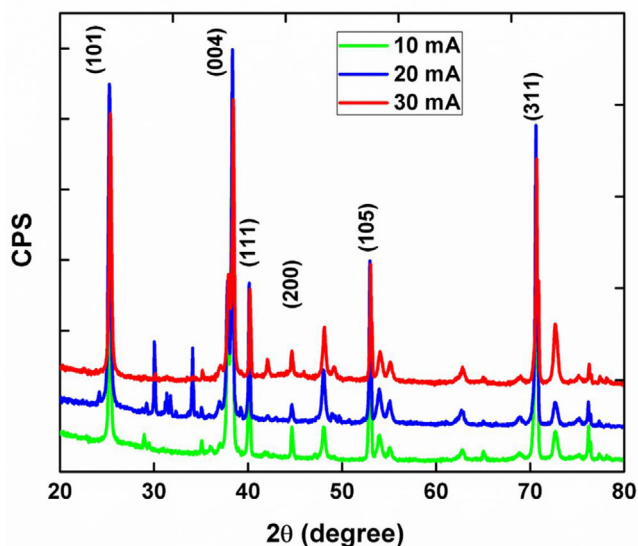


FIGURE 2 XRD pattern for the Au-sputtered TNTs at deposition currents of 10, 20, and 30 mA

band of the Au NPs on TNTs.^[29,30] Note that the plasmon band position is gradually red-shifted from the samples sputtered at 10–20 mA and then 30 mA. Even though we could not predict the change in the shape of the NPs, the

observed absorption shift can be ascribed to the increase in particle size, which increases with increasing the deposition currents (see Figure 1); larger NPs exhibit plasmonic absorbance at longer wavelength. The results indicate that all Au-decorated TNTs showcase preferably broader absorption spectra in the wavelength range from 300 to 800 nm compared to the UV dominated behavior of the bare TNTs. This can be explained based on Mei's theory and Equation (1) from the Drude model,^[30] where λ_p is the wavelength corresponding to the plasma frequency of the bulk metal, a is the radius of a spherical granule, ϵ_m is the dielectric constant of the surrounding medium, λ_{SPR} is the wavelength of surface plasmon resonance (SPR), and λ_{sb} is the wavelength of the absorbed radiation.

$$\lambda_{\text{sb}} = \lambda_p \sqrt{\frac{1 + \epsilon_m + 48\pi^2 a^2 \epsilon_m^2}{5\lambda_{\text{SPR}}^2}}. \quad (1)$$

Thus, any variation in NPs size or the dielectric constant of the surrounding medium will change the wavelength of the SPR accordingly. From Equation (1), it can be seen that the extension of the optical absorption spectra is proportional to the radius of the metal NP. Thus, enlarging the NP size would result in a red shift of the SPR band.

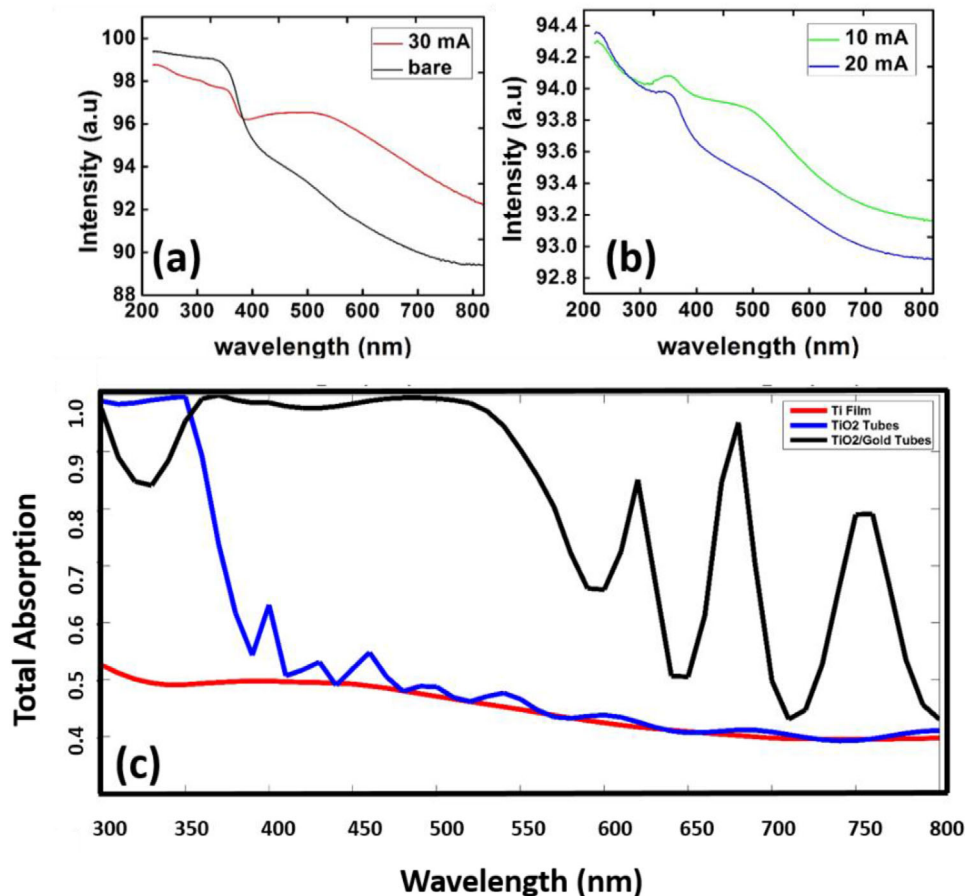


FIGURE 3 (a and b) UV-Vis spectra of bare and Au-sputtered TNTs samples and (c) the calculated total absorption for Ti film, TiO₂ nanotubes, and Au-TiO₂ nanotubes

Moreover, NPs with larger sizes would result in an enormous broadening of the resonance spectrum due to the increased contribution of multipolar excitations.^[31] This is very useful for the increment concerning photocatalytic behavior in solar energy-based applications, because the range absorbed from visible region of the solar spectrum is now expanded. Figure 3c shows total light absorption for Ti film of thickness 200 nm, TiO₂ nanotubes of height 2500 nm, inner radius 60 nm and wall thickness 10 nm deposited on the same Ti film, and TiO₂/Au nanotubes with a gold layer thickness of 25 nm along inner and outer tube surface stand on Ti film. Note that the Ti film shows the lowest absorption percentage along the entire wavelength range. Using TiO₂ nanotubes on Ti film enhances the light absorption near unity at narrow band wavelength lower than 350 nm due to the light trapping inside the TiO₂ nanotubes, followed by a decline in absorption similar to that of Ti film at higher wavelength range. Decorating the TiO₂ nanotubes with gold layer enhances the total light absorption near unity for wideband wavelength of 300–500 nm, which can be ascribed to the presence of Au that has a large absorption coefficient in the visible

light wavelength range. The other observed absorption peaks at 620, 680, and 750 nm can be ascribed to the light coupling at the dielectric–metal interface due to the strong LSPR of Au.^[32–34] Those results are in agreement with the experimentally observed absorption in Figure 3a and b.

Figure 4 illustrates the electric field profiles for (I) Ti film, (II) TiO₂ nanotubes, and (III) TiO₂/Au nanotubes at wavelengths of 300 nm and 800 nm. At 800 nm, the Ti film showed very low electric field, explaining the observed very low absorption. However, the TiO₂ nanotubes showed increased electric field inside the tubes, which is 1.5× more than that observed for the Ti film. Moreover, depositing gold on TiO₂ tubes triggers the SPR of gold and resulted in a higher electric field than that of bare TiO₂ nanotubes by 1.6×. At 300 nm, the calculated electric field was found to be very low compared to that calculated at 800 nm, because AM 1.5G has a smaller power at this wavelength.

To test the applicability of the fabricated materials, they have been used as photoanodes in water splitting systems and their performance was investigated. Figure 5a shows the variation in the obtained photocurrent for the different fabricated photoanodes. While the bare TiO₂ nanotubes

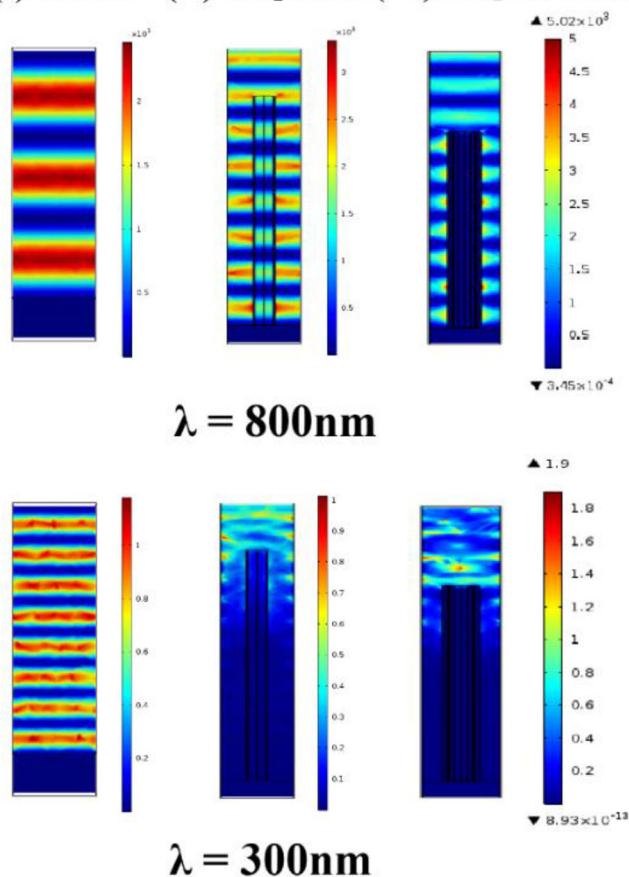
(I) Ti film (II) TiO₂ Tube (III) TiO₂/Au Tube

FIGURE 4 Electric field square profiles for (I) Ti film, (II) TiO₂ nanotubes, and (III) TiO₂/Au nanotubes at wavelengths of 300 and 800 nm

sample produced a photocurrent density of 0.403 mA/cm², the Au-decorated TNTs sputtered at 10 mA yielded the highest photocurrent density of 0.750 mA/cm² with a 86% increase in photocurrent, followed by the TNTs sputtered at 20 mA yielding a photocurrent density of 0.490 mA/cm² with only 21.5% increase in photocurrent compared to bare TNTs; TNTs sputtered at 30 mA yielded a photocurrent density 0.392 mA/cm² with a 2.8% decrease, unlike the two other sputtered samples. At the Au NPs surface, incident light induces collective oscillation of electrons. In the Au-TiO₂ interfacial region, where energy bands of TiO₂ bend in the space charge layer,^[35] the electric field of the layer may influence the oscillating electrons, which should cause the transport of the electrons to TiO₂ in bulk. Interestingly, unlike the two other TNTs samples sputtered at 10 and 20 mA, the TNTs sputtered at 30 mA, which contains the largest diameter of Au NPs, showed even a lower photocurrent density than the bare TNTs as shown in Figure 5b. This can be explained based on the fact that the deposition of an excessive amount of Au NPs would cause a shadow effect that partially block the sunlight

penetration and reduce its absorption by TiO₂.^[36] Moreover, the available surface area of the TNTs in direct contact with the aqueous electrolyte might act as electron-hole recombination centers resulting in lower photocurrent.^[37] Therefore, a careful control of the Au NPs size and density is desirable to achieve good performance. Moreover, the photoconversion efficiency (PCE) of the fabricated photoelectrodes under AM 1G illumination was calculated using Equation (2) and plotted in Figure 5c:

$$\eta(\%) = \frac{(\text{Total power output} - \text{electrical power input})}{\text{Light power input}} \times 100 = j_p \left[\frac{E_{\text{rev}}^0 - |E_{\text{appl}}|}{I_0} \right] \times 100, \quad (2)$$

where η represents the PCE, j_p is the photocurrent density (mA/cm²), $|E_{\text{appl}}|$ is the applied potential, E_{rev}^0 is the standard reversible potential, and I_0 is the incident power density (100 mW/cm²). The obtained PCE has the same trend of the photocurrent.

Stability of the photoelectrodes is one of the bottlenecks toward the realization of practical water splitting cells. To investigate the stability of the synthesized electrodes, transient photocurrent ($i-t$) measurements were performed under light on/off conditions at a constant external bias of 1 V_{Ag/AgCl} as depicted in Figure 6a. A strong photocurrent response with a sharp decay was noticed for the tested electrodes under each light on/off cycle, revealing the excellent dynamics with improved separation efficiency of the photogenerated holes and electrons.^[17] Under light-off conditions, a monotonic decay is observed for the fabricated nanotube arrays, which could likely lead to good carrier transport characteristics. Moreover, a constant photocurrent was obtained, which gives insights on the stability of the tested materials over the complete period of the test. Those observations support the utility of Au-decorated TNTs as good candidates for water splitting. To estimate the charge carrier lifetime, the photocurrent decay and response behavior was further examined (see Figure S1). According to Equation (3), the decay time constants (τ_d) can be calculated, where t is the time, I is the photocurrent, I_0 is the initial photocurrent, and τ_d is the time for the initial current to fall by 36.7%.^[38] The τ_d values of bare, 10, 20, and 30 mA Au-sputtered TNTs samples were determined and listed in Table 1:

$$I = I_0 e^{\frac{-t}{\tau_d}}. \quad (3)$$

The significant increase in charge carrier lifetime observed in the sputtered samples compared to bare TNTs is due to the fact that when larger Au NPs are brought

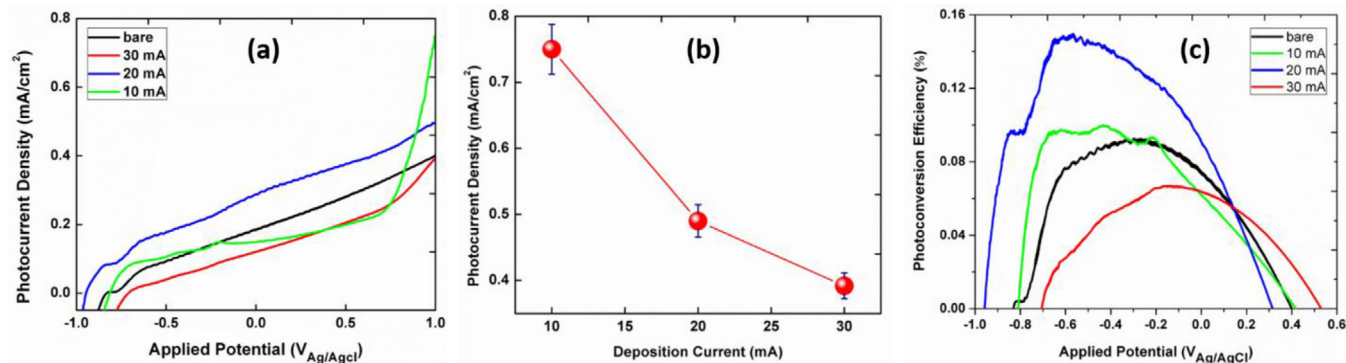


FIGURE 5 (a) I - V curves for bare and Au-sputtered samples at 10, 20, and 30 mA. (b) Variation of the maximum obtained photocurrent with the deposition current of the Au-sputtered samples, and (c) the corresponding photoconversion efficiency at AM 1.5 illumination

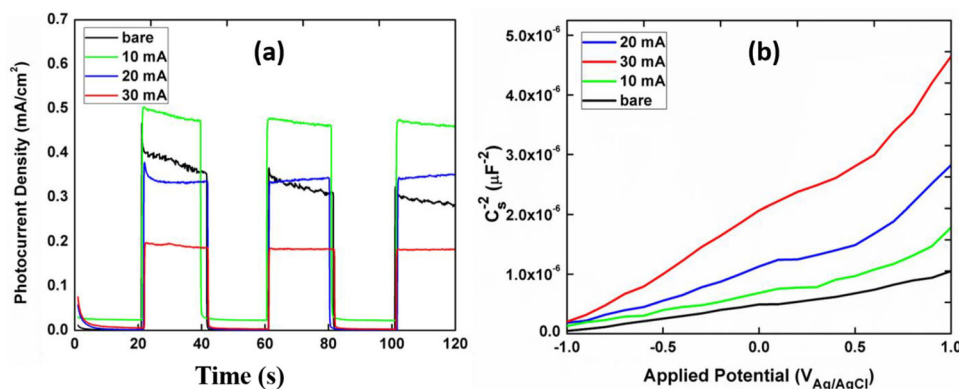


FIGURE 6 (a) Current transients at 1.0 V_{Ag/AgCl} and (b) Mott-Schottky plots for the prepared samples

into contact with TiO₂, greater amount of electrons is transferred into the Au NPs to match the Fermi levels with a more extensive space charge layer is established in the interfacial region of TiO₂, leading to a more efficient charge separation.^[39] The sample sputtered at 30 mA shows the highest charge carrier lifetime as it has the largest Au particle size and highest density; however, it showed the lowest photocurrent due to the blocking effect of this dense gold layer, which prevents the reach of energetic light photons to TiO₂ nanotubes.

The analysis of the charge carrier lifetime measurements was further confirmed using Mott-Schottky

TABLE 1 The calculated decay time constant for the fabricated samples as calculated from the exponential fitting as per Equation (3)

| Sample | τ_d (ms) | Standard error |
|--------|---------------|----------------|
| Bare | 127.0 | 0.0300 |
| 10 mA | 320.0 | 0.0600 |
| 20 mA | 812.8 | 0.0290 |
| 30 mA | 890.0 | 0.0124 |

analysis as shown in Figure 6b for bare TNTs and Au-sputtered TNT samples at 10, 20, and 30 mA. All samples exhibited positive slopes characteristic of n-type semiconductors. The donor densities (N_D) and flat band potentials (V_{FB}) were extracted from the plots at 51 Hz, where the capacitance is independent of frequency using Equation (4),^[2,40] where C_{SC} is the space charge capacitance, and $V_{Applied}$ is the applied potential bias, T is the absolute temperature of the electrochemical cell, k is the Boltzmann constant, ϵ_0 is the electric permittivity of vacuum, ϵ_r is the relative permittivity of anatase TNTs, e is the electron charge, and A is the area of the active electrode. The doping density (N_D) and flat band potential (V_{FB}) can now be obtained as the slope of the linear part and the intercept with the x-axis from of the Mott-Schottky curves:

$$\frac{1}{C_{sc}^2} = \left(\frac{2}{eN_D\epsilon_r A} \right) \left(|V_{applied} - V_{FB}| - \frac{kT}{e} \right) \quad (4)$$

Table 2 shows the flat band potential (V_{FB}) data as extracted from the Mott-Schottky curves at constant frequency of 51 Hz. The analysis indicates an increase in the donor density concentration (N_D) of the samples sputtered

TABLE 2 Donor densities (N_D) and flat band potentials (V_{FB}) as extracted from the Mott–Schottky plots

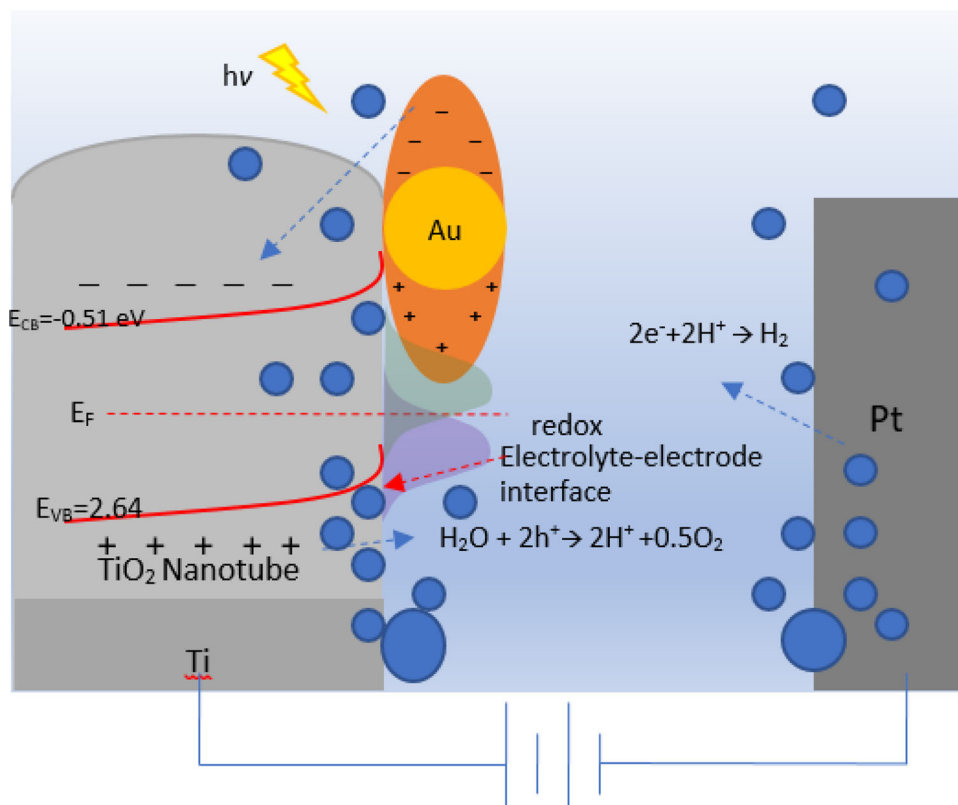
| Sample | V_{FB} (V) | $N_D \times 10^{18}$ (cm $^{-3}$) |
|--------|--------------|------------------------------------|
| Bare | −1.041 | 0.120 |
| 10 mA | −1.106 | 0.200 |
| 20 mA | −1.060 | 0.299 |
| 30 mA | −1.014 | 0.069 |

at 10 mA and 20 mA than bare TNTs, unlike the sample sputtered at 30 mA, which showed a decrease in its donor density concentration. The increase in N_D for the 10 mA and 20 mA samples and the decrease for the 30 mA sample may explain the obtained photocurrent shown in Figure 5.

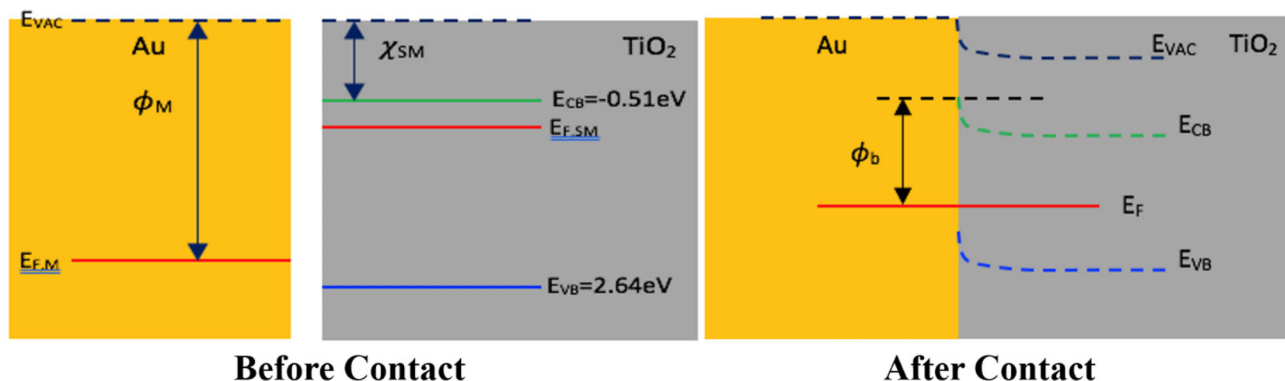
In the 10 and 20 mA Au-sputtered TNTs samples, the increase in V_{FB} compared to bare TNTs indicates higher carrier concentration in the Au–TiO₂ system. Also, the x-intercept shows negative shift, revealing very efficient charge separation and transportation. The sample sputtered at 20 mA exhibited substantially higher slope in Mott–Schottky plot compared to the bare TNT sample, revealing lower space charge capacitance (C_{sc}) at the Au–TNTs–electrolyte interface than the TNTs–electrolyte interface.^[41] The Schottky junction formed at the Au–TNTs interface is what is causing band bending at their interfaces,^[42] thus electrons can favorably step to the

conduction band of TiO₂ from the plasmon-excited Au NPs, leading to the observed more negative flat band potentials and hence an increase in the photocurrent than that of bare TNTs. In addition, at the resonance frequency, the induced internal electrostatic field by the surface charges may reduce the recombination of photogenerated charge carriers in the Au/TNTs junction region, allowing more charge carriers to participate in the intended redox reactions instead of recombining. Thus, the Mott–Schottky analysis explained the obtained high performance of the fabricated electrodes based on the enhancement in V_{FB} and N_D exhibited by the TNTs sputtered with Au NPs at 10 mA. The mechanism of electron transport and Fermi level equilibration occurred between the Fermi level of TiO₂ and Au NPs can be represented by Scheme 1.

Generally, when a semiconductor comes into contact with a metal, an energy barrier known as Schottky barrier (also Schottky diode) is developed at the interface.^[43] Typically, the Fermi level of TiO₂ is above the Fermi level of gold and close to its conduction band minimum (CBM), where some electrons can be thermally excited from electron donors to the CBM. Once TiO₂ and gold are contacted, electrons from the CBM of the TiO₂ would start to flow to the metal until an equilibrium Fermi level is built up.^[44] As the accumulation of electrons shifts the Fermi



SCHEME 1 Charge transfer mechanism at the Au–TNTs–electrolyte interface



SCHEME 2 The Fermi levels of TiO₂ and Au before and after contact

level energy of gold to more negative potentials, the resultant Fermi level of the Au–TiO₂ shifts closer to the CB of TiO₂.^[45,46] Scheme 2 illustrates the change in Fermi levels before and after contact between Au and TiO₂.

4 | CONCLUSION

In conclusion, this study shows that TiO₂ nanotubes decorated with optimized Au NPs, as confirmed via FESEM and XRD analyses, have the advantages over the bare TiO₂ nanotubes such as extended absorption in the visible region of the light spectrum, higher photoactivity, and improved life time of charge carriers, thus minimizing the recombination of e–h pairs. This was confirmed via optical modeling using FDTD. The size of the sputtered Au NPs was found to increase with increasing the sputtering deposition current. While the samples having smallest Au particle size showed the best catalytic activity, those with the largest particle size showed the least activity. However, all gold-decorated particles showed improved electron life time as compared to bare TiO₂. Upon their use as photoanodes for water splitting, the samples sputtered with Au at 10 mA showed the highest photocurrent density of 0.75 mA/cm² with an 86% increase compared to the bare TNTs (0.403 mA/cm²). The photocurrent transient measurements under light on/off conditions showed the exceptional stability of the fabricated Au-decorated TNTs. The Mott–Schottky analysis revealed an increase in the donor density concentration (N_D) for the samples sputtered at 10 mA and 20 mA than bare TNTs, unlike the sample sputtered at 30 mA, which showed a decrease in its donor density concentration. Moreover, Mott–Schottky analysis explained the obtained high performance of the fabricated electrodes based on the shift in V_{FB} and the increased N_D exhibited by the TNTs sputtered with Au NPs at 10 mA. The mechanism of electron transport and Fermi level equilibration occurred between the Fermi level of TiO₂ and Au NPs was explored and discussed in details. Therefore,

our results indicated that a careful control of the Au particle size and density is desirable to achieve good performance of the Au–TiO₂ NTs for photoelectrochemical water splitting.

ACKNOWLEDGMENTS

The financial support of this work by the American University in Cairo is highly appreciated.

CONFLICT OF INTEREST

The authors declare no conflict of interest.

DATA AVAILABILITY STATEMENT

The data will be made available upon request from the corresponding author.

ORCID

Nageh K. Allam  <https://orcid.org/0000-0001-9458-3507>

REFERENCES

1. J. Artz, T. E. Muller, K. Thenert, J. Kleinekorte, R. Meys, A. Sternberg, A. Bardow, W. Leitner, *Chem. Rev.* **2017**, *118*, 434.
2. K. E. Salem, A. M. Mokhtar, A. Abdelhafiz, N. K. Allam, *ACS Appl. Nano Mater.* **2020**, *3*, 6078.
3. S. M. Fawzy, M. A. Omar, N. K. Allam, *Sol. Energy Mater. Sol. Cells* **2019**, *194*, 184.
4. A. W. Amer, S. M. Mohamed, A. M. Hafez, S. Y. AlQaradawi, A. S. Aljaber, N. K. Allam, *RSC Adv.* **2014**, *4*, 36336.
5. N. K. Hassan, M. R. Hashim, N. K. Allam, *Chem. Phys. Lett.* **2012**, *549*, 62.
6. S. Abdel Razek, M. A. Swillam, N. K. Allam, *J. Appl. Phys.* **2014**, *115*, 194305.
7. M. Hasan, S. Tolba, N. K. Allam, *ACS Sustainable Chem. Eng.* **2018**, *6*, 16876.
8. A. H. Hegazy, N. Kinadjian, B. Sadeghimakki, S. Sivonthaman, N. K. Allam, E. Prouzet, *Sol. Energy Mater. Sol. Cells* **2016**, *153*, 108.
9. A. E. Shalan, A. N. El-Shazly, M. M. Rashad, N. K. Allam, *Nanoscale Adv.* **2019**, *1*, 2654.
10. A. A. Saleh, M. Farag, N. K. Allam, *Int. J. Hydrogen Energy* **2019**, *44*, 24418.

11. R. Ameta, S. C. Ameta, *Photocatalysis* **2016**, 17.
12. A. Fujishima, K. Honda, *Nature* **1972**, 238, 37.
13. N. K. Awad, E. A. Ashour, N. K. Allam, *J. Renew. Sustain. Energy* **2014**, 6, 022702.
14. A. M. Mohamed, A. S. Aljaber, S. Y. AlQaradawi, N. K. Allam, *Chem. Commun.* **2015**, 51, 12617.
15. R. A. Rani, A. S. Zoolfakar, A. P. O'Mullane, M. W. Austin, K. Kalantar-Zadeh, *J. Mater. Chem. A* **2014**, 2, 15683.
16. H. A. Hamedani, N. K. Allam, M. A. El-Sayed, M. A. Khaleel, H. Garmestani, F. M. Alamgir, *Adv. Funct. Mater.* **2014**, 24, 6783.
17. W. Zhou, W. Li, J.-Q. Wang, Y. Qu, Y. Yang, Y. Xie, K. Zhang, L. Wang, H. Fu, D. Zhao, *J. Am. Chem. Soc.* **2014**, 136, 9280.
18. N. Ahmed, M. Ramadan, A. A. Farghali, W. M. A. El Rouby, N. K. Allam, *Inter. J. Hydrogen Energy* **2018**, 43, 21219.
19. N. Ahmed, A. A. Farghali, W. M. A. El Rouby, N. K. Allam, *Inter. J. Hydrogen Energy* **2017**, 42, 29131.
20. A. W. Amer, M. A. El-Sayed, H. K. Allam, *J. Phys. Chem. C* **2016**, 120, 7025.
21. M. Haruta, T. Kobayashi, H. Sano, N. Yamada, *Chem. Lett.* **1987**, 16, 405.
22. M. Valden, X. Lai, D. W. Goodman, *Science* **1998**, 281, 1647.
23. M. C. Daniel, D. Astruc, *Chem. Rev.* **2004**, 104, 293.
24. L. J. Brennan, F. Purcell-Milton, A. S. Salmeron, H. Zhang, A. O. Govorov, A. V. Fedorov, Y. K. Gun'ko, *Nanoscale Res. Lett.* **2015**, 10, 38.
25. H. Kim, C. Choi, J. Khamwannah, S. Y. Noh, Y. Zhang, T.-Y. Seong, S. Jin, *J. Renew. Sustain. Energy* **2013**, 5, 53.
26. T. Lana-Villarreal, R. Gómez, *Electrochem. Commun.* **2005**, 7, 1218.
27. H. Yazid, R. Adnan, M. A. Farrukh, *Indian J. Chem., Sect. A* **2013**, 52, 184.
28. Y. Z. Zheng, Y.-Y. Xu, H.-B. Fang, Y. Wang, X. Tao, *RSC Adv.* **2015**, 5, 103790.
29. M. A. Elmoula, E. Panaitescu, M. Phan, D. Yin, C. Richter, L. H. Lewis, L. Menon, *J. Mater. Chem.* **2009**, 19, 4483.
30. U. Kreibig, M. Vollmer, *Optical Properties of Metal Clusters*, Springer Science & Business Media, Berlin, Germany **2013**.
31. U. Kreibig, M. Gartz, A. Hilger, H. Hövel. in *Fine Particles Science and Technology* (Ed: E. Pelizzetti), Springer, Berlin Germany **1996** 499.
32. P. B. Johnsonand, R. W. Christy, *Phys. Rev. B* **1974**, 12, 5056.
33. X. Wang, G. Wu, B. Zhou, J. Shen, *Materials* **2013**, 6, 2819.
34. P. B. Johnson, R. W. Christy, *Phys. Rev. B* **1972**, 6, 4370.
35. S. Link, M. A. El-Sayed, *J. Phys. Chem. B* **1999**, 103, 8410.
36. J. Li, H. Zhou, S. Qian, Z. Liu, J. Feng, P. Jin, X. Liu, *Appl. Phys. Lett.* **2014**, 104, 261110.
37. Y. Nakato, K. Ueda, H. Yano, H. Tsubomura, *J. Phys. Chem.* **1988**, 92, 2316.
38. A. F. Faid, N. K. Allam, *RSC Adv.* **2016**, 6, 80221.
39. S. Sakthivel, M. V. Shankar, M. Palanichamy, B. Arabindoo, D. W. Bahnemann, V. Murugesan, *Water Res.* **2004**, 38, 3001.
40. S. Mridha, M. Nandi, A. Bhaumik, D. Basak, *Nanotechnology* **2008**, 19, 275705.
41. R. Beranek, *Adv. Phys. Chem.* **2011**, 2011, 786759.
42. K. Yu, Y. Tian, T. Tatsuma, *Phys. Chem. Chem. Phys.* **2006**, 8(46), 5417.
43. W. H. Brattain, *Rev. Mod. Phys.* **1951**, 23, 203.
44. V. Subramanian, E. E. Wolf, P. V. Kamat, *J. Am. Chem. Soc.* **2004**, 126, 4943.
45. S. Chen, R. W. Murray, *J. Phys. Chem. B* **1999**, 103, 9996.
46. S. Chen, R. S. Ingram, M. J. Hostetler, J. J. Pietron, R. W. Murray, T. G. Schaaff, J. T. Khoury, M. M. Alvarez, R. L. Whetten, *Science* **1998**, 280, 2098.

SUPPORTING INFORMATION

Additional supporting information may be found online in the Supporting Information section at the end of the article.

How to cite this article: N. Atef, S. S. Emara, D. S. Eissa, A. El-Sayed, O. A. M. Abdelraouf, N. K. Allam. Well-dispersed Au nanoparticles prepared via magnetron sputtering on TiO₂ nanotubes with unprecedentedly high activity for water splitting. *Electrochem. Sci. Adv.* 2021;1:e2000004.
<https://doi.org/10.1002/elsa.202000004>